Chemical Science

ROYAL SOCIETY OF CHEMISTRY

EDGE ARTICLE

View Article Online
View Journal

Cite this: DOI: 10.1039/d5sc09305h

All publication charges for this article have been paid for by the Royal Society of Chemistry

Ag-triggered Co^{4+} active sites enable OH* nucleophilic attack for efficient electrocatalytic oxidation of alcohols to acids

Yu-Wei Du, Jian-Yu Zhang, Hao-Jun Luo, You Zhang, Xi-Ting Zhang, Ting Ouyang* and Zhao-Qing Liu *

Received 28th November 2025
Accepted 23rd December 2025

DOI: 10.1039/d5sc09305h

rsc.li/chemical-science

The selective oxidation of primary alcohols to carboxylic acids is a widely employed transformation in organic chemistry. However, the intrinsic mechanism by which R(Ph)–OH (R is an alkyl or phenyl) in alcohols undergoes dehydrogenation to form oxygen-rich acids remains elusive. Here, we demonstrate an efficient cooperative interface structure ($Ag/Co(OH)_2$) as an electrocatalyst. $Ag/Co(OH)_2$ significantly lowers the energy barrier of the rate-determining step ($Ph\text{-}CHO^* + OH^* \rightarrow Ph\text{-}CH(OH)_2^*$) to 0.78 eV and enhances the chemisorption energy of the Ph-CHO* intermediate to −0.89 eV, both superior to $Co(OH)_2$ ($\Delta G = 1.22$ eV, $G_{ads} = -0.72$ eV), and the faradaic efficiency for carboxylic acids reached 99.6% under mild conditions. Kinetic studies reveal the formation of Co^{4+}–O species on the composite surface, promoting the capture of OH*. Furthermore, $Ag/Co(OH)_2$ also demonstrates excellent faradaic efficiencies (ranging from 41.48% to 88.73%) in the oxidation of methanol, furfuryl alcohol, ethylene glycol, and 5-hydroxymethylfurfural to their corresponding carboxylic acids. This work provides a new idea for designing efficient and stable catalysts for electrocatalytic carboxylic acid synthesis.

Introduction

As the problems of fossil fuel depletion and environmental degradation intensify, green hydrogen energy has received much attention due to its sustainability and low environmental impact.[1,2] Driven by renewable electricity, water electrolysis is expected to be an ideal long-term low-carbon method for hydrogen production.[3,4] However, the overpotential of the anodic oxygen evolution reaction (OER) is relatively high, which limits the hydrogen production efficiency of the overall water electrolysis process. Therefore, there is an urgent need to develop alternative reaction systems with lower overpotentials.[5–8]

The catalytic oxidation of primary alcohols or primary aldehydes to carboxylic acids is one of the most important chemical transformations and is widely used in fine-chemical production.[9] Currently, industrial oxidation processes still face the challenge of thermal management under high-temperature and high-pressure conditions. If the reaction heat cannot be effectively removed, it is likely to cause local overheating, leading to catalyst deactivation, reduced selectivity, and even safety issues such as a "runaway reaction". Traditional Cr/Mn-based compounds and bromide catalysts are both toxic and costly to recover and dispose of, seriously hindering the development of green chemical processes. From the perspectives of thermodynamics and kinetics, electro-oxidation reactions involving primary alcohols or primary aldehydes can be carried out at a potential lower than that of the OER.[10,11] Therefore, converting alcohol electrocatalysis into carboxylic acids under mild conditions provides a new approach to replacing the high overpotential electrolysis water OER. This method can also be combined with renewable energy sources, simultaneously producing high-value chemicals at the anode, thereby achieving efficient conversion of electrical energy into chemical energy.[12–15] Electrocatalytic alcohol oxidation reactions involve multiple electrochemical steps (*e.g.* proton-coupled electron transfer (PCET)) and chemical steps (*e.g.* C–C cleavage).[16,17] Through different reaction pathways, various products can be obtained. Furthermore, the electronic structure and steric hindrance of different alcohol molecules (such as aromatic alcohols and aliphatic alcohols) also affect the catalytic rate.[18] Accordingly, developing efficient catalysts to regulate the oxidation processes of various alcohols and obtain the desired high-value chemicals remains a significant challenge.

$Co(OH)_2$, as a highly promising anode catalyst, is rich in surface hydroxyl groups that can dehydrogenate from Co^{2+}–OH to form Co^{3+}–O species, acting as a proton mediator to efficiently drive the PCET process during alcohol oxidation.[19–22] Furthermore, the Co^{3+}-oxo species over CoOOH formed after the reconstruction of $Co(OH)_2$ play a key role in the benzyl alcohol oxidation reaction (AOR, using BA as the substrate) process.[23–25]

School of Chemistry and Chemical Engineering, Institute of Clean Energy and Materials, Key Laboratory for Clean Energy and Materials, Huangpu Hydrogen Innovation Center, Guangzhou University, Guangzhou 510006, P. R. China. E-mail: ouyt@gzhu.edu.cn; lzqgzhu@gzhu.edu.cn

However, $Co(OH)_2$ has a limited range for regulating the adsorption strengths of the intermediates, which can easily lead to the desorption or over-oxidation of the reacting intermediates. In this process, the adsorption behavior of the reacting molecules on the catalyst directly affects the electro-oxidation efficiency. Notably, constructing a coupled active-metal-transition-metal compound support is an effective strategy to enhance the electrocatalytic activity.[26,27] The construction of such heterogeneous interfaces enhances the electrical conductivity[28] and optimizes the local coordination environments of the active sites and regulates the adsorption behavior,[29–31] thus significantly improving the catalytic performance. Recently, nano-Ru-modified $Ni(OH)_2$ enhanced the adsorption capacity for phenol by regulating the electronic structure of Ru sites, thereby achieving its efficient conversion into *p*-quinone.[32] By utilizing the thermal and electronic plasmonic effects of Ag, Ag-modified CoV-LDH@G with Mott–Schottky heterojunctions showed significantly improved OER performance.[33] In addition, Pd-Cu_2O nanoparticles, with the enhanced adsorption of CO intermediates, achieved a significant improvement in the methanol oxidation reaction (MOR) activity.[34] Certainly, it is crucial to enhance the catalytic performance for the catalytic oxidation of alcohols by rationally modulating the adsorption energies of key reaction intermediates on the catalyst surface.

In this work, we demonstrate a simple and feasible electrocatalytic strategy for the oxidation of primary alcohols over a silver-modified cobalt hydroxide ($Ag/Co(OH)_2$) electrocatalyst. The AOR was selected as a model reaction to evaluate the

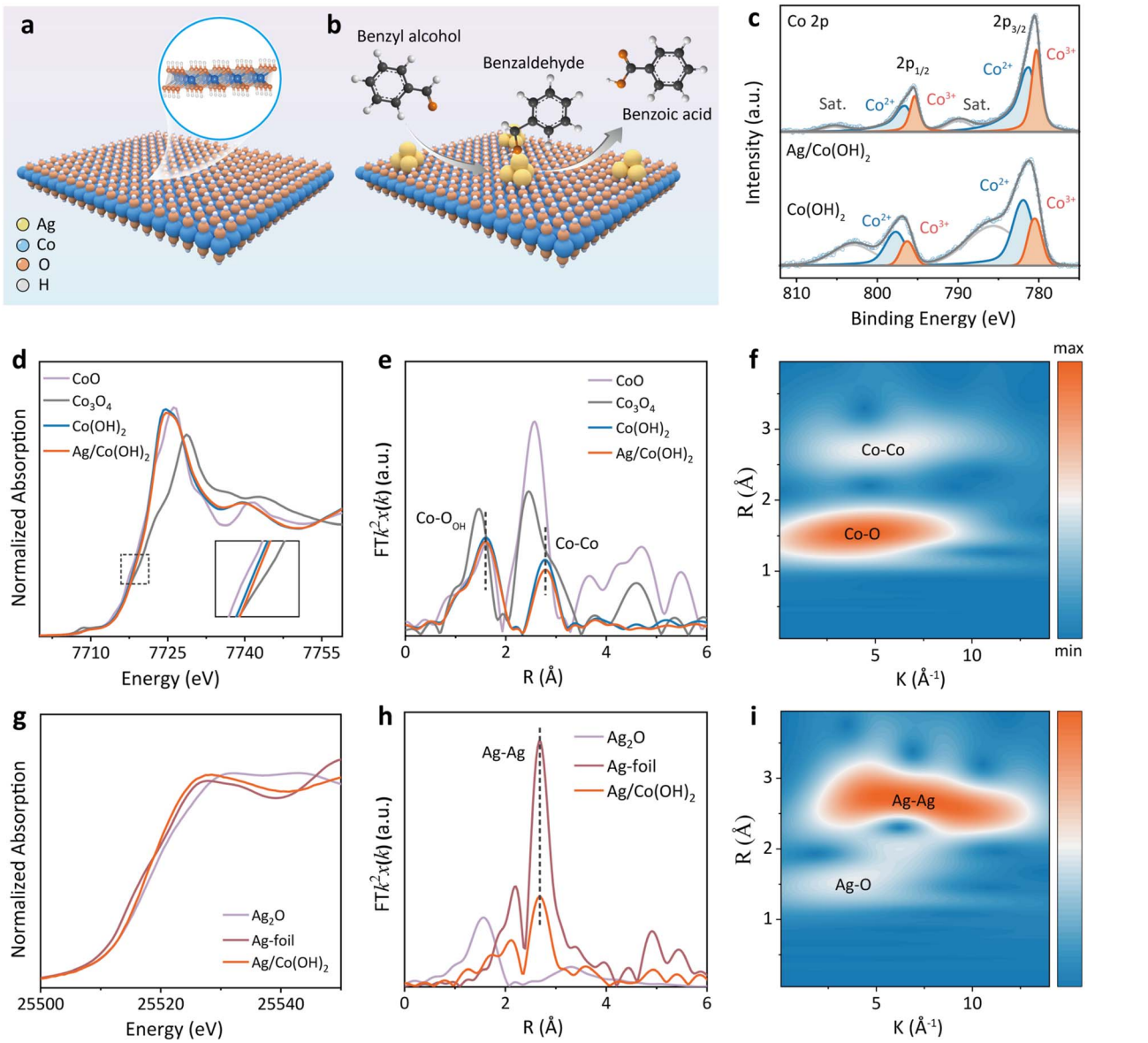

Fig. 1 (a) A diagram of $Co(OH)_2$. (b) A schematic diagram of the electro-oxidation of BA on the surface of $Ag/Co(OH)_2$. (c) Co 2p XPS spectra. (d) Co K-edge XANES spectra and (e) the corresponding EXAFS spectra. (f) The contour map of Co K-edge WT-EXAFS. (g) Ag K-edge XANES spectra and (h) the corresponding EXAFS spectra. (i) The contour map of Ag K-edge WT-EXAFS (to avoid the analytical effects of nickel foam on cobalt, the catalyst was grown on carbon cloth for XRD, XANES and FT-EXAFS measurements).

catalytic performance. A series of electrochemical tests in alkaline solution revealed that Ag/$Co(OH)_2$ exhibits high activity for the AOR, with high selectivity for the generation of benzoic acid (BAC) products (Fig. 1a and b). Experimental characterization and theoretical calculations show that silver modification could effectively modulate the surface charge transfer kinetics of the catalyst and induce the formation of high-valence active sites (Co^{4+}–O). More importantly, Ag/$Co(OH)_2$ exhibits superior performance over $Co(OH)_2$ in terms of both the activation barrier of the rate-limiting step of the oxidation reaction (the combination of Ph-CHO* and OH*; 0.78 eV *vs.* 1.22 eV) and the adsorption energy of Ph-CHO at the interface (−0.89 eV *vs.* −0.72 eV), thereby achieving an faradaic efficiency (FE) of 99.6% for BAC under mild conditions (1.45 V *vs.* RHE). Impressively, the unique cooperative interface mechanism of Ag/$Co(OH)_2$ can adapt to the electronic structures and spatial configurations of different alcohol molecules, also affording universal oxidation activity for other primary alcohols (methanol, furfuryl alcohol, ethylene glycol, and 5-hydroxymethylfurfural: the corresponding FEs for the acids can reach 41.48% to 88.73%).

Results and discussion

Catalyst synthesis and characterization

Ag/$Co(OH)_2$ was synthesized on nickel foam (NF) *via* electrodeposition and spontaneous redox methods. Scanning electron microscopy (SEM) images show that $Co(OH)_2$ is uniformly plated on NF with a dense nanosheet morphology. With the introduction of Ag, the sample is transformed into a complex structure of nanoparticles and ultrathin nanosheets stacked on top of each other (Fig. S1). High-resolution transmission electron microscopy (HRTEM) imaging exhibits the presence of both Ag (111) and $Co(OH)_2$ (100) stripes corresponding to Ag/$Co(OH)_2$ (Fig. S2). Also, XRD spectra show crystallographic peaks consistent with Ag and $Co(OH)_2$ (PDF# 04-0783 and PDF# 51-1731) (Fig. S3), indicating the successful synthesis of Ag/$Co(OH)_2$. The quantitative determination of Ag and Co in the catalyst was performed using inductively coupled plasma optical emission spectrometry (ICP-OES, Table S1). The results indicate that the content of Ag in the material is relatively low (5.19 at%). Energy-dispersive spectroscopy (EDS) further confirms that the elements Co and O are uniformly distributed, while Ag appears as blocky aggregates on top of Co (Fig. S4). The surface composition and electronic states of $Co(OH)_2$ before and after Ag modification were examined by X-ray photoelectron spectroscopy (XPS). Compared to $Co(OH)_2$, Ag modification promotes the formation of Co^{3+} and oxygen vacancies (Fig. 1c and S5).

The X-ray absorption near-edge structure (XANES) spectra of Co are also displayed (Fig. 1d and S6a). The absorption edges of the white line peaks correlate with the 1s → 4p electronic transitions, reflecting the valence state information of the catalysts. Ag/$Co(OH)_2$ and $Co(OH)_2$ show white line peaks that are higher than CoO and lower than Co_3O_4 (wherein Co has an average oxidation state of +2.67), which implies that the average oxidation state of the Co atoms in Ag/$Co(OH)_2$ and $Co(OH)_2$ is between +2 and +3. Also, the higher intensity of the white line peak for Ag/$Co(OH)_2$ confirms that the introduction of Ag increases the oxidation state of Co, which is consistent with the results from XPS. The Fourier transform extended X-ray absorption fine structure (FT-EXAFS) spectra show two distinct peaks at 1.6 Å and 2.8 Å, corresponding to the coordination structures of Co–O and Co–Co (Fig. 1e and S6b). The corresponding EXAFS fitting images in K and R space are illustrated (Fig. S7 and S8), and detailed numerical values are presented (Table S2). EXAFS analysis using wavelet transform (WT) provides the same evidence (Fig. 1f and S9).[35] It is noteworthy that the coordination number of Co–O decreases from 6.2 to 5.9 after Ag introduction, suggesting the formation of oxygen vacancies, which matches the results of O 1s XPS analysis (Fig. S5a). In addition, Ag was also subjected to K-edge XANES measurements. The results indicate that the valence state of Ag lies between 0 and +1, and the main coordination structure is Ag–Ag (Fig. 1g–i, S10–S12, and Table S3).

Performance evaluation of the alcohol oxidation reaction

BA was selected as a model substrate for alcohol oxidation, and the performance of the catalysts in the AOR was evaluated using cobalt-based material as the anode and a platinum sheet electrode as the cathode. Linear scanning voltammetry (LSV) analysis was first performed. As shown in Fig. 2a, Ag/$Co(OH)_2$ exhibits the earliest onset potential and a higher current density. The oxidation peak at 1.21 V *vs.* RHE was identified as the Co^{2+}/Co^{3+} oxidation peak, which was related to the oxidation of $Co(OH)_2$ to CoOOH. For $Co(OH)_2$, the oxidation peak appeared at 1.25 V *vs.* RHE, suggesting that Ag modification promotes the electro-oxidation of Co^{2+}–OH to Co^{3+}–OH. Cyclic voltammetry (CV) curves exhibit the same results (Fig. 2b and S13).

Within the potential range of 1.2–1.6 V *vs.* RHE, the AOR current density of Ag/$Co(OH)_2$ is higher than that of $Co(OH)_2$ (Fig. 2c), further confirming that the promoting effect of Ag modification enhances the electrocatalytic activity. In addition, the Tafel slopes over a potential range are displayed in Fig. 2d. The Tafel value of Ag/$Co(OH)_2$ (325 mV dec^{-1}) is lower than that of $Co(OH)_2$ (501 mV dec^{-1}). These results, together with electrochemical impedance spectroscopy (EIS) measurements at the open-circuit potential, indicate that the introduction of Ag could accelerate the reaction kinetics (Fig. S14). In general, the double-layer capacitance (C_{dl}) is directly related to the electrochemically active surface area (ECSA), with a larger C_{dl} value indicating a larger ECSA. The C_{dl} values of Ag/$Co(OH)_2$ are significantly higher than those of $Co(OH)_2$ (Fig. S15), indicating that the introduction of silver effectively enhanced the ECSA of the material, thereby improving its catalytic performance. Moreover, the C_{dl} values of both catalysts measured in 1.0 M KOH are higher than their corresponding values in 1.0 M KOH + 0.1 M BA. This might be due to the adsorption of BA on the catalyst surface at the measurement potential, partially covering active sites available for double-layer charging. The zeta potential reflects the potential at the slipping plane between a particle and a solution. This is affected by pH, as a change in

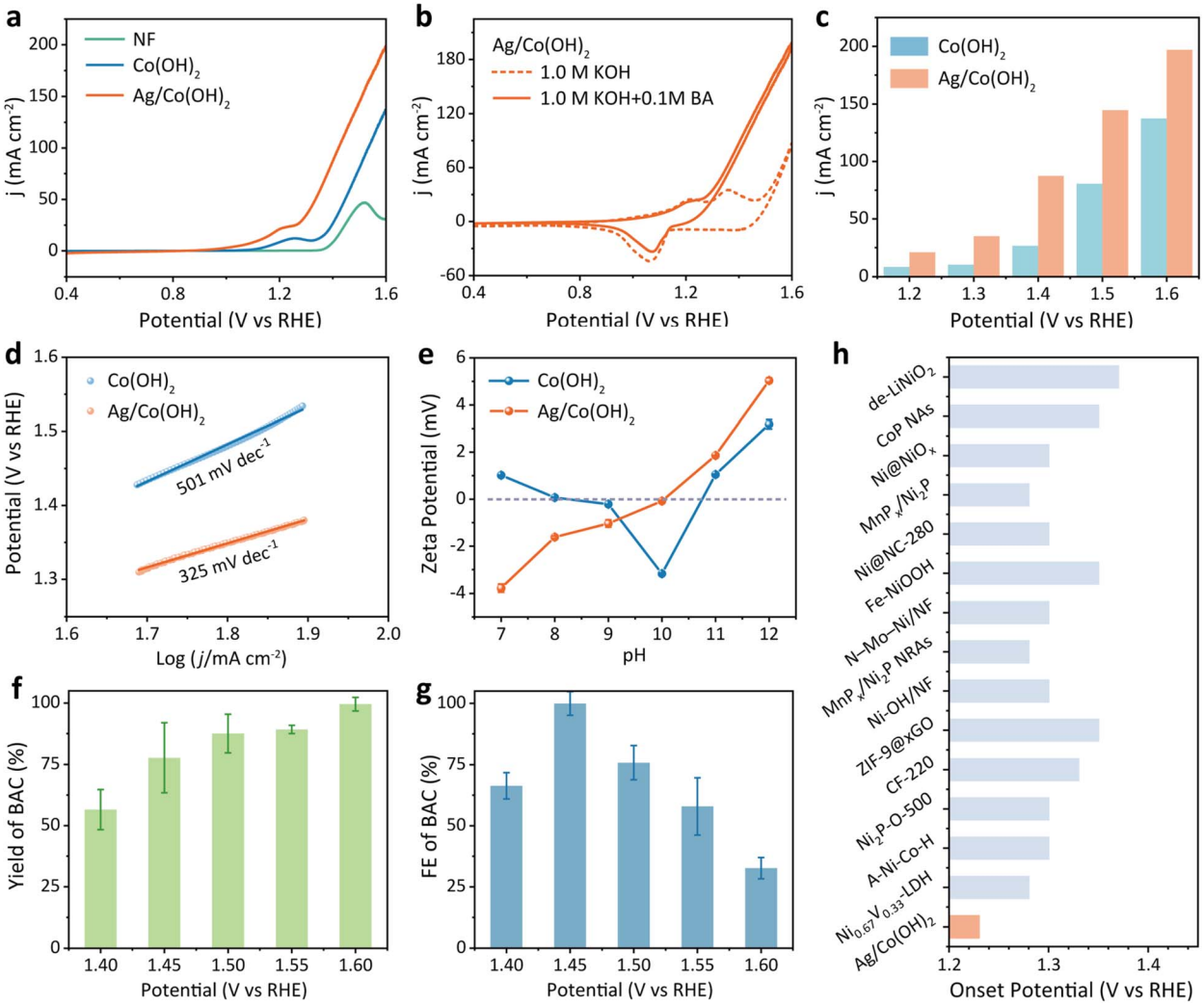

Fig. 2 (a) LSV curves of NF-supported $Co(OH)_2$ and $Ag/Co(OH)_2$ catalysts in 1.0 M KOH + 0.1 M BA. (b) CV curves of the $Ag/Co(OH)_2$ catalyst in 1.0 M KOH + 0.1 M BA (solid line) and 1.0 M KOH (dotted line) (c) A comparison of the current densities of $Co(OH)_2$ and $Ag/Co(OH)_2$ at different potentials. (d) Tafel slopes of $Co(OH)_2$ and $Ag/Co(OH)_2$. (e) The zeta potentials of $Co(OH)_2$ and $Ag/Co(OH)_2$ under different pH conditions. (f and g) The yields and FEs of BAC at different voltages during the AOR on $Ag/Co(OH)_2$. (h) A comparison of the AOR onset potential of the $Ag/Co(OH)_2$ catalyst with reported state-of-the-art catalysts.

pH alters the protonation state of the functional groups on a particle's surface.[36,37] The pH at which the zeta potential is zero is the isoelectric point (IEP). As seen in Fig. 2e, the IEP of $Ag/Co(OH)_2$ (~pH 10) is higher than that of $Co(OH)_2$ (~pH 9), maintaining a more positive and stable zeta potential in the pH > 10 range. Notably, the zeta potential of $Co(OH)_2$ exhibits a non-monotonic change (positive → negative → positive) with an increase in pH, potentially due to surface remodelling under strongly alkaline conditions, whereas $Ag/Co(OH)_2$ shows a monotonically positive shift. This suggests that introducing Ag enhances the stability of the hydroxyl groups on the surface of $Co(OH)_2$ in alkaline environments and increases the positive electronegativity of the surface by optimizing the interfacial charge, thus promoting the adsorption of OH^-.

The electrocatalytic activities of $Co(OH)_2$ and $Ag/Co(OH)_2$ in the AOR were investigated using 1.0 M KOH + 0.1 M BA as the electrolyte, and the post-oxidation products were detected by gas chromatography-mass spectrometry (GC-MS). The electrolyte after 12 h of reaction at 1.4 V *vs.* RHE was collected and analysed (Fig. S16). Clearly, the $Co(OH)_2$-catalyzed product has the presence of both benzaldehyde (BAD) and BAC, while the $Ag/Co(OH)_2$ product is dominated by BAC, indicating that modification with Ag might affect the desorption of intermediate products and thus achieve the highly selective oxidation of BA to BAC. The amount of Ag modification of the catalyst was optimized using LSV and GC-MS data (Fig. S17 and S18). When the concentration of Ag^+ is 13.3 mM, the catalyst shows the best AOR performance at high potential with faster product formation (larger GC-MS peak area). In order to further quantify the reactants and products, standard curves for BA, BAD and BAC were made (Fig. S19). The yields and FEs of BAC in the voltage range of 1.4–1.6 V *vs.* RHE are shown in Fig. 2f and g. The yield increases with an increase in potential; however, the FE decreases with an increase in potential;

a possible reason is that at higher potentials, the OER competes with the AOR and the charge is dispersed. Therefore, it is necessary to select a suitable potential to minimize the effects of OER competition. 1.45 V *vs.* RHE is the optimal potential, where the yield of BAC reaches 77.7% and the FE is 99.6%. After 12 h of the AOR reaction, the structure of the Ag/$Co(OH)_2$ catalyst was characterized (Fig. S20–S22). The XRD results show that the intensity of the characteristic diffraction peaks of Ag metal weakened, indicating that Ag undergoes a chemical-state or dispersion-state transformation under the electrocatalysis conditions. EDS mapping and XPS analysis confirm that the Ag element does not leach out, and it remains uniformly distributed. The intensity of the oxygen vacancy-related peak in the O 1s XPS spectrum increases significantly after the reaction, indicating a higher concentration of surface oxygen defects. These oxygen vacancies and the highly dispersed Ag species form a more efficient catalytic interface, thereby supporting the performance of Ag/$Co(OH)_2$ in

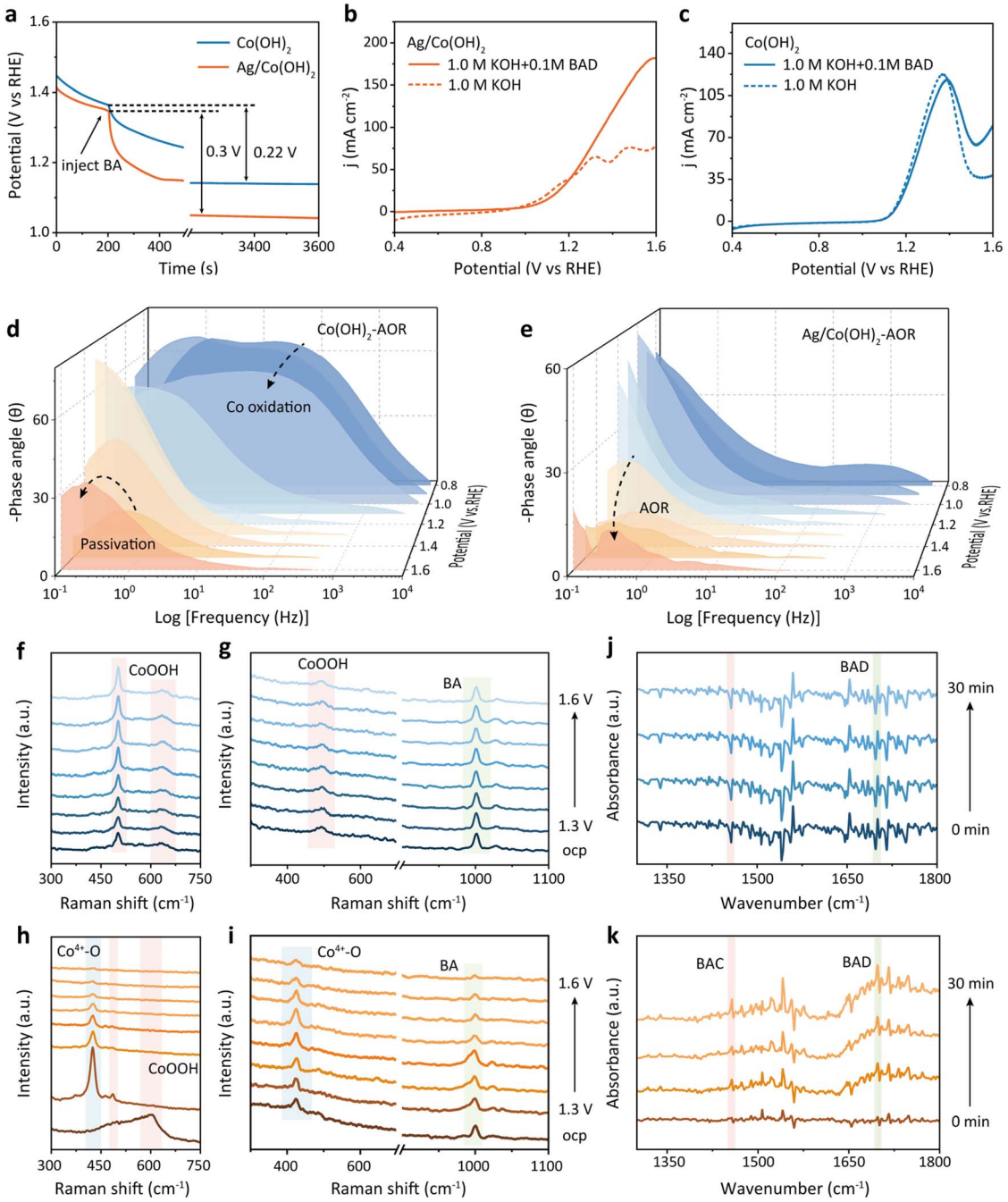

Fig. 3 (a) The OCP changes of $Co(OH)_2$ and Ag/$Co(OH)_2$ catalysts in 1.0 M KOH after 0.1 M BA is injected. (b and c) LSV curves of Ag/$Co(OH)_2$ and $Co(OH)_2$ catalysts in 1.0 M KOH with and without 0.1 M BAD. (d and e) *In situ* impedance-phase angles of $Co(OH)_2$ and Ag/$Co(OH)_2$ during electro-oxidation at various potentials (0.8–1.6 V *vs.* RHE). *In situ* Raman spectra of $Co(OH)_2$ (f and g) and Ag/$Co(OH)_2$ (h and i) during the OER (1.0 M KOH) and AOR (1.0 M KOH + 0.1 M BA), respectively. (j and k) *In situ* FT-IR spectra of $Co(OH)_2$ and Ag/$Co(OH)_2$ during the AOR.

maintaining a high FE during the long-term reaction. The Ag/$Co(OH)_2$ catalyst exhibits a lower onset potential compared to other reported AOR catalysts (Fig. 2h and Table S4).[11,13,38–49]

Mechanistic elucidation

To further investigate the adsorption behavior of BA on the catalyst, open-circuit potential testing was performed. As seen in Fig. 3a, the potential drop of Ag/$Co(OH)_2$ (0.30 V) is higher than that of $Co(OH)_2$ (0.22 V) upon the addition of 0.1 M BA at 200 s, indicating that the BA better adsorbs on Ag/$Co(OH)_2$. This helps to optimize the initial reaction steps and facilitate the subsequent PCET process. To further verify that modification with Ag could modulate the product selectivity of the AOR, the catalytic performance of the catalysts in 1.0 M KOH + 0.1 M BAD was also investigated. Ag/$Co(OH)_2$ exhibits higher oxidizing activity toward BAD compared with $Co(OH)_2$, which promotes further oxidation of the intermediate product (Fig. 3b and c). Next, the oxidation processes occurring at the catalyst interface during the OER and AOR were monitored and analyzed using *in situ* EIS. For $Co(OH)_2$, the phase angle gradually decreases with increasing voltage (0.8–1.1 V *vs.* RHE) in the high frequency region, which is associated with a phase transition process from $Co(OH)_2$ to CoOOH inside the catalyst. When the voltage exceeds 1.4 V *vs.* RHE, the phase angle in the low-frequency region gradually decreases, corresponding to the progression of the OER. Upon the addition of BA, the phase transition in the low-frequency region was advanced to 1.3 V *vs.* RHE (Fig. 3d and S23), consistent with the LSV results in Fig. 2a. As seen in Fig. 3e, Ag/$Co(OH)_2$ displays a smaller phase angle at all potentials, which indicates faster reaction kinetics, *i.e.*, faster charge transfer, at its surface. Moreover, during the AOR, $Co(OH)_2$ shows a passivation signal at a high potential of 1.6 V *vs.* RHE, which did not occur at the Ag/$Co(OH)_2$ interface. This might be due to the slower AOR kinetics at the $Co(OH)_2$ interface compared to Ag/$Co(OH)_2$. At high oxidation potentials, such kinetic limitation promotes the accumulation of OH^+ oxide species, eventually leading to the formation of a CoOOH passivation layer.

In order to investigate the interfacial structure evolution of the catalysts during the reaction process, *in situ* Raman spectroscopy tests were performed (Fig. 3f–i and S24). During the OER with the Ag/$Co(OH)_2$ catalyst, two characteristic peaks at 484 cm^{-1} and 602 cm^{-1} are observed at the OCP, which may be attributed to the E_g and A_{1g} modes of CoOOH, respectively.[10,35] With an increase in the applied potential, a new peak appears at

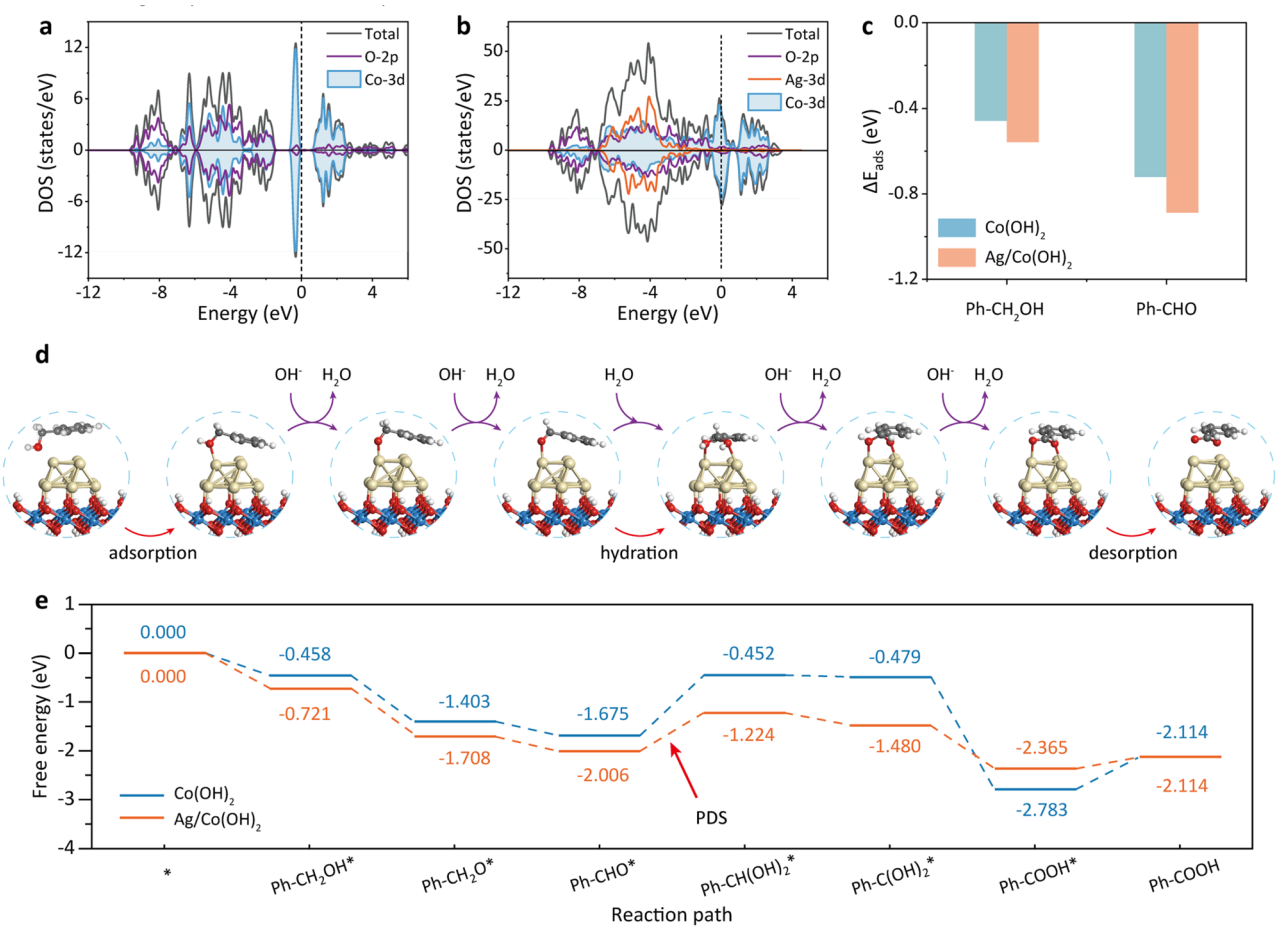

Fig. 4 (a and b) The calculated density of states of (a) $Co(OH)_2$ and (b) Ag/$Co(OH)_2$ surfaces. (c) A comparison of the adsorption energies of Ph-CH_2OH (BA) and Ph-CHO (BAD) on different catalysts. (d) Adsorption configurations and (e) Gibbs free energy diagrams of the BA to BAC process on Ag/$Co(OH)_2$. Atoms are color-coded as follows: Co (blue), O (red), Ag (yellow), C (gray), and H (white).

425 cm^{-1}, and the signal could be clearly assigned to the characteristic vibrations of CoO_2 or CoO_2-like species,[17,20] indicating that the catalyst surface undergoes a transition from a Co^{3+} to a Co^{4+} oxidation state. Notably, when BA is introduced into the electrolyte, the intensity of the Co^{4+}-related signal at 425 cm^{-1} gradually decreases with increasing potential, suggesting that the oxidation of BA consumes Co^{4+} active species, leading to their reduction to a lower valence state. This result is further corroborated by the attenuation of the intensity of the characteristic peak of the benzene ring at 1000 cm^{-1},[50] confirming the depletion of BA molecules in the reaction. In contrast, the Raman spectra of $Co(OH)_2$ catalysts in the same potential interval (OER and AOR systems) do not show significant changes, and their peak positions and intensities remain stable, indicating that the material does not undergo any obvious valence or phase structure transitions under the reaction conditions. These results highlight the key regulatory role of Ag modification on the electronic structure and catalytic activity of $Co(OH)_2$. The adsorption behavior of the catalyst during the AOR process was investigated by *in situ* Fourier transform infrared spectroscopy (FTIR) at a constant potential of 1.45 V *vs.* RHE (Fig. 3j and k). The characteristic peak at 1697 cm^{-1} is attributed to the C=O stretching vibration of BAD.[51–53] After Ag modification, a new peak, gradually intensifying over time, at 1540 cm^{-1} is observed, which could be attributed to the asymmetric stretching vibration of the –C(O)OH group in BAC.[54] This phenomenon confirms that Ag/$Co(OH)_2$ could further oxidize the Ph-CHO intermediate to BAC.

Density functional theory calculations

In order to deeply investigate the reaction mechanism and C–H bond activation mechanism of the AOR over Ag/$Co(OH)_2$, density functional theory (DFT) calculations were performed. First, $Co(OH)_2$ (100) pure surface and Ag-modified $Co(OH)_2$ (100) surface models were constructed for simulating the interfacial effects in the AOR reaction (Fig. S25). Density of states (DOS) analysis reveals that compared to pure $Co(OH)_2$, the d-electrons of Co in Ag/$Co(OH)_2$ are more concentrated near the Fermi level, suggesting a higher valence electron density, improved conductivity, and enhanced electron transfer capabilities (Fig. 4a and b).[55,56] Moreover, the d-electron orbitals of Co in Ag/$Co(OH)_2$ exhibit greater dispersion, which means that it has a wider bonding range and the electrons could participate in the reaction more easily. Additionally, the calculated results show that the adsorption energies (E_{ads}) of both BA and BAD on the Ag/$Co(OH)_2$ surface are significantly higher than those on the pure $Co(OH)_2$ surface (Fig. 4c and Tables S5, S6), and this result is in agreement with the data from the open-circuit potential and LSV tests (Fig. 3a–c). This suggests that Ag/$Co(OH)_2$ has a stronger adsorption affinity for BAD, leading to the lower desorption of BAD, which is more favorable for the subsequent reaction.

In order to gain insight into the effect of the introduction of Ag on catalyst performance, we investigated in detail the reaction mechanism of the conversion from BA to BAC and the corresponding energy changes. The reaction starts with the co-adsorption of Ph-CH_2OH and OH* in the two models, which produces Ph-CHO* after two dehydrogenation steps. Subsequently, Ph-CHO* hydrates in water to form Ph-$CH(OH)_2^*$, which then undergoes dehydrogenation to produce Ph-COOH. In the reaction pathway, the potential-determining step (PDS) is the hydration process, with energy barriers of 1.223 eV and 0.782 eV at the $Co(OH)_2$ and Ag/$Co(OH)_2$ sites, respectively (Fig. 4d, e, S26, and Tables S7, S8). The introduction of Ag significantly reduces the PDS energy barrier, thus promoting the formation of key intermediates.

Substrate scope expansion

Having established that Ag can enhance the adsorption of Ph-CHO* intermediates and promote highly selective acid production from alcohols, we further demonstrated the oxidative versatility of the catalyst using other monohydric alcohols (methanol (MeOH), furfuryl alcohol (FFA), ethylene glycol (EG), and 5-hydroxymethylfurfuryl aldehyde (HMF)) (Fig. 5). The catalytic applicability is initially assessed by LSV, followed by the definitive verification of carboxylic acid formation *via* ^1H and ^{13}C nuclear magnetic resonance (NMR) spectroscopy and high-performance liquid chromatography (HPLC) (Fig. S27–S30). Notably, no characteristic peaks corresponding to *CHO intermediates were detected, suggesting that potential aldehyde intermediates were rapidly oxidized under the catalytic conditions. Based on the corresponding standard curves (Fig. S31–S34), quantitative calculations were performed for the conversion rates of alcohols, the yields of acids, and their purity. The average values obtained from three parallel experiments are

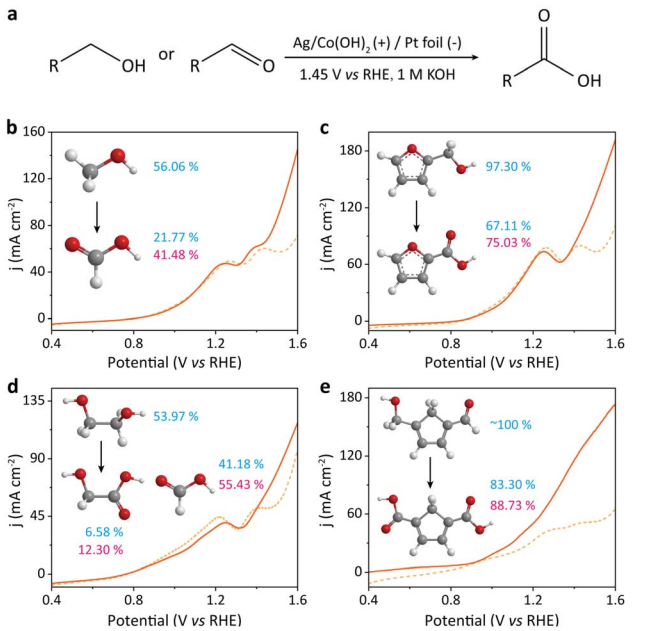

Fig. 5 (a) A schematic diagram depicting the pathway for the generation of the primary acid at the electrode. The electro-oxidative conversion of various substrates into corresponding carboxylic acids catalyzed by Ag/$Co(OH)_2$: (b) MeOH to FA; (c) FFA to FUA; (d) EG to EA and FA; and (e) HMF to FDCA. The conversion rate of the substrate and the yield of the acid are indicated in blue font, while the FE of the acid is shown in pink font.

given (Fig. 5 and S35), and the standard deviations are listed (Table S9). At 1.45 V *vs.* RHE, Ag/$Co(OH)_2$ exhibits excellent catalytic performance in the oxidation reactions of several alcohols: MeOH conversion reaches 56.06% with a formic acid (FA) yield of 21.77% (FE: 41.48%); FFA shows 97.30% conversion yielding 67.11% furoic acid (FUA; FE: 75.03%); EG achieves 53.97% conversion, producing both glycolic acid (GA; yield: 6.58%, FE: 12.30%) and FA (yield: 41.18%, FE: 55.43%); while HMF exhibits near-quantitative conversion (~100%) with a 2,5-furandicarboxylic acid yield of 83.30% (FDCA; FE: 88.73%). These results show that the designed Ag-modified $Co(OH)_2$ catalysts exhibit excellent versatility for the synthesis of other carboxylic acids.

Conclusions

In summary, we present a highly active and low-cost Ag-modified $Co(OH)_2$ catalyst for the efficient electrocatalytic oxidation of alcohols to carboxylic acids. By enhancing conductivity and forming high-valence Co active sites (Co^{4+}–O), the AOR oxidation current of Ag/$Co(OH)_2$ significantly increases, resulting in rapid AOR kinetics over a wide potential range and achieving a BAC FE of 99.6% at 1.45 V *vs.* RHE. *In situ* electrochemical experimental results and DFT calculations indicate that Ag modification facilitates electron transfer from alcohol to the catalyst and strengthens the adsorption and activation of the key intermediate (Ph-CHO*). The rate-determining step for Ag/$Co(OH)_2$ is the transformation from Ph-CHO* + OH* to Ph-$CH(OH)_2^*$, which has an energy barrier of 0.782 eV. This barrier is significantly lower than that on $Co(OH)_2$ (1.223 eV), indicating the high selectivity toward BAC achieved with the Ag/$Co(OH)_2$ catalyst. Furthermore, Ag/$Co(OH)_2$ can also catalyze the conversion of MeOH, FFA, EG and HMF to the corresponding carboxylic acids, with FEs ranging from 41.48% to 88.73%, demonstrating the universality of this catalyst strategy for regulating the adsorption energies of intermediates.

Author contributions

Z. Liu and T. Ou Yang: conceived and supervised the research, funding acquisition, writing – review & editing. Y. Du: conducted the experiments, analyzed the data, and wrote the manuscript. J. Zhang, H. Luo and Y. Zhang: assisted with the material synthesis and characterization. X. Zhang: supported supervising and reviewing the manuscript. All authors contributed to the interpretation of the results.

Conflicts of interest

There are no conflicts to declare.

Data availability

The authors confirm that the data supporting the findings of this work are available within the article and its supplementary information (SI). Supplementary information: details of Experimental section including materials and electrochemical measurement; zeta potential measurements; standard curves of product analysis, calculated faradaic efficiencies; *in situ* FT-IR; *in situ* Raman; XAFS measurement; calculation method. See DOI: https://doi.org/10.1039/d5sc09305h.

Acknowledgements

This work was financially supported by National Natural Science Foundation of China (No. 22379033, U24A20541 and 22278094), Guangdong Basic and Applied Basic Research Foundation (No. 2025B1515020046), Guangzhou Science and Technology Program (No. 2025A03J0011), Basic and Applied Basic Research Program of Guangzhou (No. 2024A03J0236), and Science and Technology Research Project of Guangzhou (No. 202201020214). We would like to thank Analysis and Test Center of Guangzhou University for their technical support.

Notes and references

1 N. Johnson, M. Liebreich, D. M. Kammen, P. Ekins, R. McKenna and I. Staffell, *Nat. Rev. Clean Technol.*, 2025, **1**, 351–371.
2 S. W. Boettcher, *Chem. Rev.*, 2024, **124**, 13095–13098.
3 X. Zhang, C. Cao, T. Ling, C. Ye, J. Lu and J. Shan, *Adv. Energy Mater.*, 2024, **14**, 2402633.
4 R. Wan, T. Yuan, L. Wang, B. Li, M. Liu and B. Zhao, *Nat. Catal.*, 2024, **7**, 1288–1304.
5 J. Li and H. Duan, *Chem*, 2024, **10**, 3008–3039.
6 X. Huang, O. Akdim, M. Douthwaite, K. Wang, L. Zhao, R. J. Lewis, S. Pattisson, I. T. Daniel, P. J. Miedziak, G. Shaw, D. J. Morgan, S. M. Althahban, T. E. Davies, Q. He, F. Wang, J. Fu, D. Bethell, S. McIntosh, C. J. Kiely and G. J. Hutchings, *Nature*, 2022, **603**, 271–275.
7 Z. Yang, L. Chen, Y. Yin, C. Wei, Z. Xue and T. Mu, *Energy Environ. Sci.*, 2024, **17**, 8801–8809.
8 L. Chen, Z. Yang, Q. Hu, C. Yan, Y. Yao, Y. Bao, Z. Pei, T. Mu and Z. Xue, *Angew. Chem., Int. Ed.*, 2025, **137**, e202511868.
9 J. Zhang, Y. Shen, Z. Wu, X. Zhang, J. Kang, Y. Wu, S. Zhang, S. Chen, G. Wang, H. Zhang, H. Yin and H. Zhao, *Angew. Chem., Int. Ed.*, 2025, **64**, e202423109.
10 Y. Lin, Y. Chen, H. Ren, Y. Sun, J. Chen, M. Wu and Z. Li, *Adv. Funct. Mater.*, 2024, **34**, 2404594.
11 H. Huang, C. Yu, X. Han, H. Huang, Q. Wei, W. Guo, Z. Wang and J. Qiu, *Energy Environ. Sci.*, 2020, **13**, 4990–4999.
12 Z. Wang, J. Li, Q. Zhang, C. Wu, H. Meng, Y. Tang, A. Zou, Y. Zhang, R. Ma, X. Lv, Z. Yu, S. Xi, J. Xue, X. Wang and J. Wu, *Angew. Chem., Int. Ed.*, 2024, **63**, e202411517.
13 S. Li, S. Wang, Y. Wang, J. He, K. Li, J. B. Gerken, S. S. Stahl, X. Zhong and J. Wang, *Nat. Commun.*, 2025, **16**, 266.
14 J. N. Hausmann, P. V. Menezes, G. Vijaykumar, K. Laun, T. Diemant, I. Zebger, T. Jacob, M. Driess and P. W. Menezes, *Adv. Energy Mater.*, 2022, **12**, 2202098.
15 S. Han, L. Sun, D. Fan and B. Liu, *Nat. Commun.*, 2025, **16**, 3426.
16 Y. Yan, J. Zhong, R. Wang, S. Yan and Z. Zou, *J. Am. Chem. Soc.*, 2024, **146**, 4814–4821.

17 L. Wu, Q. Wu, Y. Han, D. Zhang, R. Zhang, N. Song, Y. Fang, H. Liu, M. Wang, J. Chen, A. Du, K. Huang and X. Yao, *J. Am. Chem. Soc.*, 2025, **147**, 18033–18043.
18 Z. Li, Y. Yan, S.-M. Xu, H. Zhou, M. Xu, L. Ma, M. Shao, X. Kong, B. Wang, L. Zheng and H. Duan, *Nat. Commun.*, 2022, **13**, 147.
19 L. Zhang, Y. Liu, L. Li, T. Wu, Q. Wu, J. Z. Y. Seow, X. Lin, S. Sun, L. Tannesia, K. Tang, D. Shao, S. Xi, X. Guo and Z. J. Xu, *Energy Environ. Sci.*, 2025, **18**, 5622–5631.
20 X. Huang, Y. Guo, Y. Zou and J. Jiang, *Appl. Catal., B*, 2022, **309**, 121247.
21 C. Jing, T. Yuan, L. Li, J. Li, Z. Qian, J. Zhou, Y. Wang, S. Xi, N. Zhang, H.-J. Lin, C.-T. Chen, Z. Hu, D.-W. Li, L. Zhang and J.-Q. Wang, *ACS Catal.*, 2022, **12**, 10276–10284.
22 K. Xiang, D. Wu, X. Deng, M. Li, S. Chen, P. Hao, X. Guo, J.-L. Luo and X.-Z. Fu, *Adv. Funct. Mater.*, 2020, **30**, 1909610.
23 Y. Q. Zhu, H. Zhou, J. Dong, S. M. Xu, M. Xu, L. Zheng, Q. Xu, L. Ma, Z. Li, M. Shao and H. Duan, *Angew. Chem., Int. Ed.*, 2023, **62**, e202219048.
24 S. Liu, S. Dou, J. Meng, Y. Liu, Y. Liu and H. Yu, *Appl. Catal., B*, 2023, **331**, 122709.
25 Z. He, J. Hwang, Z. Gong, M. Zhou, N. Zhang, X. Kang, J. W. Han and Y. Chen, *Nat. Commun.*, 2022, **13**, 3777.
26 R. Chen, S. Chen, L. Wang and D. Wang, *Adv. Mater.*, 2024, **36**, 2304713.
27 H. Wang, Z. Gao, B. Sun, S. Mu, F. Dang, X. Guo, D. Ma and C. Shi, *Chem Catal.*, 2023, **3**, 100768.
28 S. Liu, J. Lu, X. Yu, H. Pang, Q. Zhang and H. S. Park, *eScience*, 2025, 100378.
29 C. Lee, K. Shin, C. Jung, P.-P. Choi, G. Henkelman and H. M. Lee, *ACS Catal.*, 2020, **10**, 562–569.
30 S. Liu, B. Tian, X. Xu, X. Wang, P. Ran, Y. Sun, J. Wu, A. Qiu, F. Wang, L. Tang, J. Ma and M. Ding, *ACS Catal.*, 2024, **14**, 9476–9486.
31 A.-Z. Li, X. Wang, S. Li, B.-J. Yuan, X. Wang, R.-P. Li, L. Zhang, B.-J. Li and H. Duan, *J. Am. Chem. Soc.*, 2025, **147**, 10493–10503.
32 F. Liu, W. Chen, T. Wang, J. Zhang, D. Yang, Y. Dai, G. Liu, J. Zhou, S. Wang and X. Guan, *Angew. Chem., Int. Ed.*, 2025, **64**, e202415438.
33 X. Lu, Z. Ma, Y. Chang, S. Wang, X. Li, D. Xu, J. Bao and Y. Liu, *Adv. Mater.*, 2024, **36**, 2313057.
34 X. Zhang, L. Hui, F. He and Y. Li, *J. Am. Chem. Soc.*, 2025, **147**, 436–445.
35 A. Moysiadou, S. Lee, C.-S. Hsu, H. M. Chen and X. Hu, *J. Am. Chem. Soc.*, 2020, **142**, 11901–11914.
36 Q. Yan, C. Lian, K. Huang, L. Liang, H. Yu, P. Yin, J. Zhang and M. Xing, *Angew. Chem., Int. Ed.*, 2021, **60**, 17155–17163.
37 S.-L. Xu, W. Wang, Y. Song, R. Tang, Z.-H. Hu, X. Zhou and H.-Q. Yu, *Water Res.*, 2025, **270**, 122851.
38 L. Chen, C. Yu, X. Song, J. Dong, Y. Han, H. Huang, X. Zhu, Y. Xie and J. Qiu, *Small*, 2024, **20**, 2306410.
39 Y. Han, C. Yu, H. Huang, Q. Wei, J. Dong, L. Chen and J. Qiu, *SmartMat*, 2024, **5**, e1206.
40 S. Chongdar, A. Ghosh, R. Bal and A. Bhaumik, *J. Mater. Chem. A*, 2024, **12**, 233–246.
41 L. Ming, X.-Y. Wu, S.-S. Wang, W. Wu and C.-Z. Lu, *Green Chem.*, 2021, **23**, 7825–7830.
42 Y. Zhao, Y. Yan, Y. Wang, E. M. Björk, S. Wang, T. Li, Y. Lu, D. Wang, P. Schaaf, X. Wang and G. Guo, *Mater. Today Energy*, 2025, **48**, 101780.
43 J. Wan, X. Mu, Y. Jin, J. Zhu, Y. Xiong, T. Li and R. Li, *Green Chem.*, 2022, **24**, 4870–4876.
44 L. Wei, M. D. Hossain, M. J. Boyd, J. Aviles-Acosta, M. E. Kreider, A. C. Nielander, M. B. Stevens, T. F. Jaramillo, M. Bajdich and C. Hahn, *ACS Catal.*, 2023, **13**, 4272–4282.
45 J. Zhong, Y. Shen, P. Zhu, S. Yao and C. An, *Nano Res.*, 2023, **16**, 202–208.
46 X. Wen, K. Chen, Y. Su, K. Xiong, P. Fan, J. Wu, C. Liu, Q. Qu and L. Li, *Chem. Eng. J.*, 2024, **493**, 152510.
47 R. Li, P. Kuang, S. Wageh, A. A. Al-Ghamdi, H. Tang and J. Yu, *Chem. Eng. J.*, 2023, **453**, 139797.
48 S. Ye, Z. Chen, G. Zhang, W. Chen, C. Peng, X. Yang, L. Zheng, Y. Li, X. Ren, H. Cao, D. Xue, J. Qiu, Q. Zhang and J. Liu, *Energy Environ. Sci.*, 2022, **15**, 760–770.
49 S. Li, H. Tian, W. Luo, H. Wu, W. Sun, X. Cui and J. Shi, *Small*, 2025, **21**, 2408507.
50 J. Y. Loh, F. M. Yap, T. J. Siang, X. Zeng and W.-J. Ong, *Small*, 2024, **21**, 2409331.
51 Z. Zhang, B.-L. Leng, S.-N. Zhang, D. Xu, Q.-Y. Li, X. Lin, J.-S. Chen and X.-H. Li, *J. Am. Chem. Soc.*, 2024, **146**, 27179–27185.
52 H. Zhang, Y. Gao, S. Meng, Z. Wang, P. Wang, Z. Wang, C. Qiu, S. Chen, B. Weng and Y.-M. Zheng, *Adv. Sci.*, 2024, **11**, 2400099.
53 J. Yu, P. Zhang, L. Li, K. Li, G. Zhang, J. Liu, T. Wang, Z.-J. Zhao and J. Gong, *Nat. Commun.*, 2022, **13**, 7909.
54 R. Liu, W. Tu, A. Pei, W.-H. Huang, Y. Jia, P. Wang, D. Liu, Q. Wu, Q. Qin, W. Zhou, L. Zhou, K. Yan, Y. Zhao and G. Chen, *J. Am. Chem. Soc.*, 2025, **147**, 10339–10348.
55 J. J. Masana, J. Xiao, H. Zhang, X. Lu, M. Qiu and Y. Yu, *Appl. Catal., B*, 2023, **323**, 122199.
56 H. Li, K. Gan, R. Li, H. Huang, J. Niu, Z. Chen, J. Zhou, Y. Yu, J. Qiu and X. He, *Adv. Funct. Mater.*, 2023, **33**, 2208622.